

Is Λ CDM on the run? Reconciling the CMB with the Lyman- α Forest

Malcolm Fairbairn,^{1,*} Lucien Heurtier,^{1,†} and María Olalla Olea-Romacho^{1,‡}

¹ *Theoretical Particle Physics and Cosmology, King's College London, Strand, London WC2R 2LS, United Kingdom*

We present new constraints on the scale dependence of the primordial power spectrum by combining *Planck*, ACT DR6, SPT-3G and eBOSS Lyman- α forest data, extending sensitivity to smaller comoving scales. While ACT results previously indicated a mild preference for positive running of the spectral index, our joint analysis constrains both the running α_s and its running β_s . Including eBOSS markedly tightens these constraints, yielding a $> 2\sigma$ indication of nonzero α_s and/or β_s , challenging predictions from vanilla slow-roll inflation potentials. Comparing reconstructed spectral parameters with theoretical models, we find that inflationary potentials with localised dips, bumps, or oscillations better reproduce the observed scale dependence. We release the public PIPE code to test arbitrary inflationary potentials against these datasets.

Introduction. — Cosmic inflation provides the leading explanation for the initial conditions of our Universe, accounting for its homogeneity and flatness while generating the primordial fluctuations observed in the cosmic microwave background (CMB) and large-scale structure (LSS) [1, 2]. Yet, the physical origin of this accelerated expansion—and the detailed shape of the inflaton potential that may drive it—remain unknown.

Since its first proposal in the early 80s [3], CMB observatories and LSS surveys have enabled increasingly precise tests of inflation. The beautiful successes of *WMAP* [4] and *Planck* [5] revealed the structure of the CMB fluctuations on small scales, providing evidence for a Universe fully consistent with the Λ CDM hypothesis – a spatially flat Universe containing only baryons, cold dark matter and a cosmological constant, with a flat or nearly flat dimensionless power spectrum of scalar curvature perturbations that can be modelled with a single power law $\Delta_{\mathcal{R},\Lambda\text{CDM}}^2(k) \equiv A_s(k/k_*)^{n_s-1}$. Cosmic inflation generally predicts a spectral index n_s close to unity, indeed, *Planck* measured $n_s = 0.9651 \pm 0.0044$ at the pivot scale $k_* = 0.05 \text{ Mpc}^{-1}$ [5], confirming the success of the Λ CDM model. In single-field slow-roll inflation, the dynamics of the inflaton—uniquely determined by the shape of the inflaton potential—predict small but generic deviations from this form of the primordial power spectrum (PPS), which can be captured by Taylor-expanding its logarithm around the pivot scale as

$$\begin{aligned} \ln \Delta_{\mathcal{R}}^2(k) &\equiv \ln A_s + (n_s - 1) \ln \left(\frac{k}{k_*} \right) \\ &+ \frac{\alpha_s}{2} \ln \left(\frac{k}{k_*} \right)^2 + \frac{\beta_s}{6} \ln \left(\frac{k}{k_*} \right)^3 \\ &+ \dots \end{aligned} \quad (1)$$

where α_s and β_s denote the running and running-of-the-running of the spectral index.

While CMB observations tightly constrain this spectrum around the pivot scale, their sensitivity decreases at smaller scales, limiting their ability to detect mild departures from a power-law spectrum. To probe these smaller scales, we incorporate data from eBOSS [6], which measured $\sim 2 \times 10^5$ quasar spectra with detectable Lyman- α forests. These observations probe wavenumbers around $k \sim 1 \text{ h Mpc}^{-1}$, providing complementary information on the amplitude and slope of the matter power spectrum in a regime inaccessible to the CMB alone. Notably, eBOSS measurements suggest a suppression of small-scale power that is difficult to reconcile with the nearly scale-invariant spectrum preferred by CMB data. In particular, Rogers and Poulin [7] found that combining *Planck* 2018 data with the eBOSS Lyman- α forest flux power spectrum leads to a statistically significant tension with the assumption of a single powerlaw primordial spectrum, with a reported 5σ preference for suppression at small scales. Their analysis indicates deviations from scale invariance for $k \gtrsim 0.1 \text{ h Mpc}^{-1}$, consistent with a negative running of the spectral index, and yields a best-fit value of $\alpha_s = -0.0108 \pm 0.0022$.

This stands in contrast to recent CMB measurements from ACT DR6 [8, 9], which mildly favour a positive running, $\alpha_s > 0$. These experiments probe smaller angular scales than *Planck*, extending CMB sensitivity to higher wavenumbers and thereby bridging the gap with the eBOSS Lyman- α forest regime. Taken together, these datasets and the eBOSS results appear to pull the preferred shape of the primordial spectrum in opposite directions, suggesting a more complex scale dependence. This CMB–Lyman- α tension provides strong motivation to go beyond the leading-order power-law expansion and examine the second derivative of the spectral index, β_s , in addition to α_s .

In this *letter*, assuming the small-scale suppression is primordial [10] rather than a late-time effect, we perform a joint analysis of *Planck*, ACT DR6, SPT-3G [11], and eBOSS data to constrain both α_s and β_s . We show that including eBOSS substantially tightens these constraints and leads to a preference for nonzero values, challenging predictions from simple slow-roll potentials. We fur-

* Email address: malcolm.fairbairn@kcl.ac.uk

† Email address: lucien.heurtier@kcl.ac.uk

‡ Email address: maria.olalla.olea.romacho@kcl.ac.uk

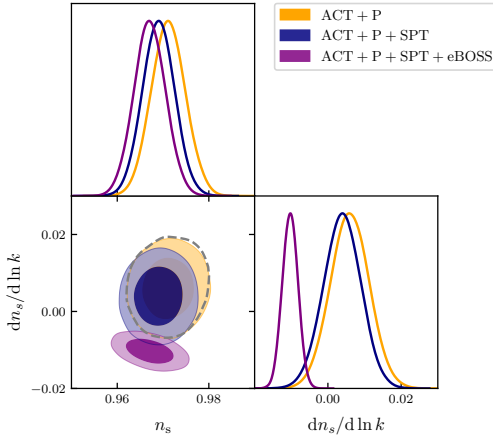


FIG. 1. Joint and marginalized posterior probability distributions for n_s and its running $\alpha_s = dn_s/d \ln k$, derived from the three likelihood combinations analysed in this work. Shaded contours represent the 68% and 95% credible regions. The dashed grey curve corresponds to the ACT+P constraint from Ref. [9], obtained when fitting only α_s .

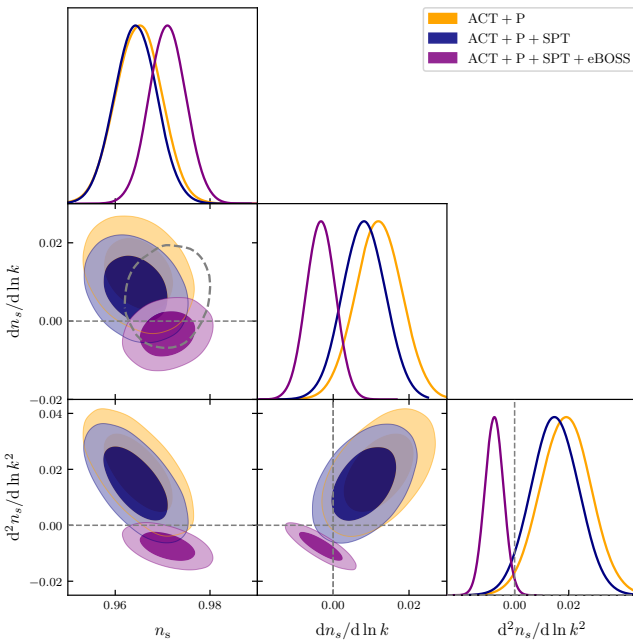


FIG. 2. Same as FIG. 1 but including $\beta_s = d^2 n_s / d \ln k^2$. Median values and corresponding 68% credible intervals for these parameters are reported in the Supplemental Material.

ther test specific inflationary scenarios—including monomial, axion-monodromy, and potentials with localised features—to identify models capable of reproducing the observed suppression of small-scale power while remaining consistent with state-of-the-art CMB measurements. Finally, we release the public PIPE code, designed to evaluate arbitrary inflationary potentials against combinations of current CMB and LSS datasets, enabling systematic tests of inflationary physics beyond the standard

paradigm.

Power Spectrum Running. — *Likelihood.* To constrain the PPS, we use the most recent likelihoods from *Planck* [5] and the ACT DR6 Lite likelihood released by the ACT collaboration [8, 9].¹ Our setup follows the *Planck*-ACT (P-ACT) cut configuration described in Ref. [8], which combines large-scale Planck data with high-resolution ACT measurements. Specifically, we include the low- ℓ TT spectrum from Planck [12] and the low- ℓ EE spectrum from the Srol12 reanalysis [13], while at high multipoles we use ACT DR6 CMB-only data in the *Planck*-ACT cut, retaining *Planck* data only up to $\ell = 1000$ in TT and $\ell = 600$ in TE/EE. ACT data dominate at smaller scales, covering the range $600 < \ell < 6500$ in TT, TE, and EE, with foregrounds marginalised over. We also include the foreground-marginalised likelihood SPT-3G D1 Lite published recently by SPT [11].² Similarly to Ref. [7], to account for Lyman- α constraints on the matter power spectrum, we use a compressed 2D Gaussian likelihood derived from the eBOSS (Sloan Digital Sky Survey Data Release 14; SDSS DR14) Lyman- α forest flux power spectrum [6] and tabulated in Ref. [14]. All the cosmological information in the eBOSS flux power spectrum can be compressed into two parameters: the amplitude $\Delta_{\text{lin}}^2 \equiv \frac{k^3 P_{\text{lin}}(k_p, z_p)}{2\pi^2}$ and the tilt $n_{\text{lin}} \equiv \left. \frac{d \ln P_{\text{lin}}(k, z)}{d \ln k} \right|_{k_p, z_p}$ of the linear matter power spectrum $P_{\text{lin}}(k, z)$, evaluated at the pivot redshift $z_p = 3$ and wavenumber $k_p = 0.009 \text{ s km}^{-1}$. The mean values of Δ_{lin}^2 and n_{lin} are respectively 0.310 and -2.340, the standard deviations are respectively 0.020 and 0.006, and the correlation coefficient is 0.512 [14].

Monte Carlo Markov Chain. We perform Monte Carlo Markov Chain (MCMC) sampling using the publicly available code Cobaya [15] interfaced with the Boltzmann solver CAMB [16], to extract constraints on the amplitude and shape of the PPS given in Eq. (1). We perform two separate analyses: one where we sample the scalar amplitude $\ln(10^{10} A_s)$ and spectral index n_s at the pivot scale $k_* = 0.05 \text{ Mpc}^{-1}$, together with the running α_s , and one in which we also include the running of the running β_s . These parameters are varied jointly with the remaining four baseline ΛCDM parameters: the optical depth to reionization τ , the physical baryon density ω_b , the physical cold dark matter density ω_c , and the angular size of the sound horizon θ_s . In addition, we vary the nuisance parameters T_{cal} and E_{cal} , which account for the absolute calibration of the temperature and polarisation spectra, respectively. For all parameters, we adopt the same flat priors as used by the ACT collaboration in the ACT-DR6.02 “nrun” analysis.³

To ensure convergence, we run multiple chains (using

¹ <https://github.com/ACTCollaboration/DR6-ACT-lite>

² https://github.com/SouthPoleTelescope/spt_candl_data

³ https://lambda.gsfc.nasa.gov/product/act/act_dr6.02_act_dr6.02_chains_nrun_get.html

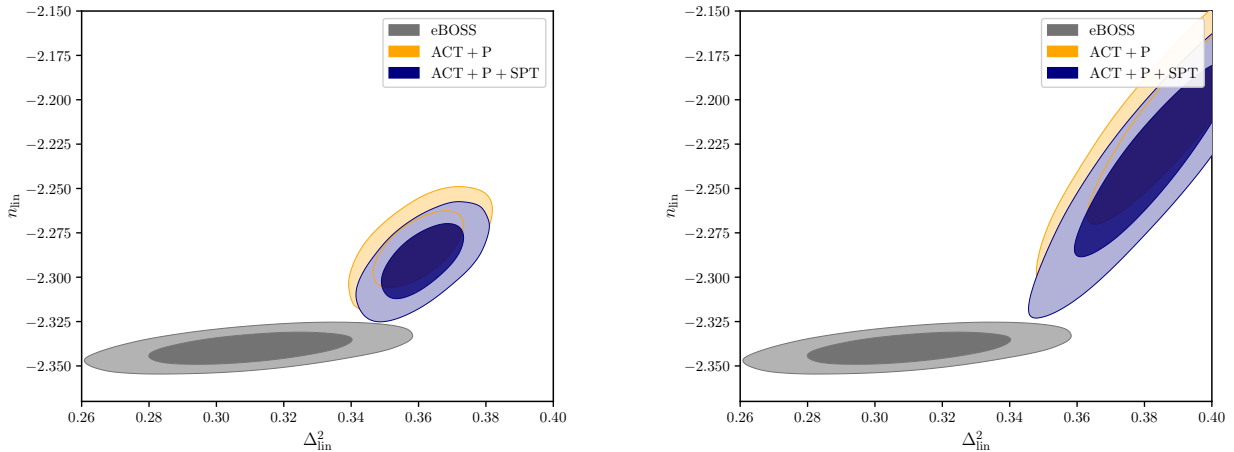


FIG. 3. Posteriors for $(\Delta_{\text{lin}}^2, n_{\text{lin}})$ when includin the running (left panel) and running-of-the-running (right panel) of the spectral index.

12 CPUs when including only α_s in the analysis, and 15 CPUs when also including β_s in parallel and monitor the Gelman-Rubin R statistic, requiring $R - 1 < 0.05$ for all sampled parameters.

Results. Fig. 1 shows the constraints obtained when allowing only the running of the spectral index. Adding eBOSS data tightens the bounds and shifts both n_s and α_s ; the data disfavours $\alpha_s = 0$ at $> 2\sigma$, already hinting at higher-order scale dependence. Fig. 2 extends to the running-of-the-running, β_s , showing 68 % and 95 % credible regions from *Planck*+ACT DR6 (yellow), +SPT-3G (blue), and +eBOSS Ly- α (purple). The inclusion of eBOSS sharply contracts the contours and drives them along the α_s - β_s toward more negative values, with $\beta_s = 0$ disfavoured at about 2σ . The corresponding shift of n_s toward larger values suggests a slightly bluer tilt once small-scale Ly- α data are included. Central values and credible intervals are given in the Supplemental Material.

Using posteriors in the $(\Delta_{\text{lin}}^2, n_{\text{lin}})$ plane (Fig. 3), we quantified tensions between CMB and eBOSS datasets with the `tensiometer` package [17] (see Supplemental Material for details). The combined ACT+P+SPT data increase the CMB–eBOSS discrepancy beyond the previously reported 4.9σ for *Planck* alone [7]. Allowing for running reduces this to $\sim 3 - 3.3\sigma$ (vs. $\sim 1\sigma$ with *Planck* only), and including β_s further lowers it to $\sim 2.8 - 3\sigma$.

The trend reflects competing preferences: *Planck* yields a mildly negative central value of α_s , and ACT DR6 favours $\alpha_s > 0$, whereas eBOSS requires a strong suppression of small-scale power, corresponding to $\alpha_s < 0$. Consequently, CMB data collectively prefer $\alpha_s > 0$ and $\beta_s > 0$, while eBOSS drives both negative. ACT and SPT therefore accentuate the *Planck*–eBOSS tension, and allowing a constant negative β_s only partially alleviates it—it steepens the small-scale suppression but cannot recover the positive running preferred by the CMB.

Implications for Inflation — Recent constraints favouring higher values of the scalar spectral index have

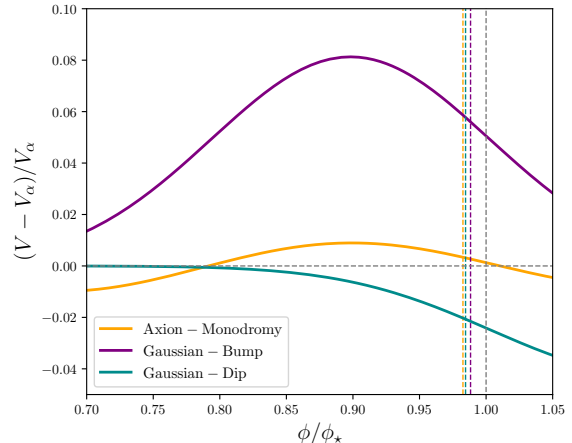


FIG. 4. Relative modulation of the potential $(V - V_\alpha)/V_\alpha$, as compared to the baseline model $V_\alpha \equiv V_0|\phi/M_p|^\alpha$, for each set of best-fit parameters (V_0, α, \dots) listed in TABLE I. Vertical, coloured, dashed lines denote the field value corresponding to where perturbations exit the horizon at the eBOSS scale.

revived interest in inflationary scenarios beyond canonical plateau potentials. Models such as exponential α -attractors [18–20], Starobinsky [21], and Higgs inflation [22] typically struggle to accommodate $n_s \gtrsim 0.97$ [23–27]. This trend motivates the exploration of alternatives that favour potentials approaching the plateau polynomially rather than exponentially [23]. We therefore consider several single-field potentials, beginning with a monomial baseline $V_\alpha = V_0|\phi/M_p|^\alpha$, where α controls the slope and $\alpha < 1$ is preferred by recent data [9]. We then introduce localised or oscillatory deviations to capture transient dynamics.

Gaussian bumps and dips. Transient features—e.g. from localized particle production or modulations [28–31]—can modify the dynamics of $\dot{\phi}$, impact CMB ob-

Dataset	Model	$\log_{10} V_0$	α	$\log_{10} A$	$\phi_0 [M_{\text{Pl}}]$	$\sigma [M_{\text{Pl}}]$	γ	$\log_{10} f$	p_f	$\ln \mathcal{L}_{\text{KDE}}$	$\ln \pi_r$	$\ln \mathcal{L}$
ACT+P	Powerlaw	-9.3565	0.3935	—	—	—	—	—	—	32.032	2.835	34.867
	Powerlaw+Bump	-9.5142	0.1698	-3.8106	-4.287	0.161	—	—	—	34.024	3.603	37.626
	Powerlaw+Dip	-9.5350	0.1951	-2.3266	-5.594	0.599	—	—	—	34.024	3.603	37.626
	Axion-Monodromy	-9.5085	0.1662	-4.2186	—	—	7.416	-1.053	0.0053	34.051	3.603	37.654
+SPT	Powerlaw	-9.3829	0.3067	—	—	—	—	—	—	31.730	3.334	35.065
	Powerlaw+Bump	-9.4408	0.0826	-1.5910	-4.096	0.938	—	—	—	35.099	3.601	38.699
	Powerlaw+Dip	-9.3917	0.0316	-1.3712	-1.071	0.988	—	—	—	35.099	3.601	38.699
	Axion-Monodromy	-9.5012	0.1566	-3.2910	—	—	0.492	0.077	0.829	35.099	3.603	38.702
+eBOSS	Powerlaw	-10.2659	1.6448	—	—	—	—	—	—	6.859	-19.494	-12.636
	Powerlaw+Bump	-10.2095	0.8137	-1.0900	-8.282	0.964	—	—	—	37.305	3.603	40.908
	Powerlaw+Dip	-9.8199	0.5068	-1.3842	-7.776	0.774	—	—	—	37.305	3.603	40.908
	Axion-Monodromy	-9.6943	0.3672	-1.7747	—	—	24.70	-0.372	-0.0060	37.305	3.603	40.908

TABLE I. Best-fit parameters, KDE log-likelihood ($\ln \mathcal{L}_{\text{KDE}}$), and tensor prior contribution ($\ln \pi_r$) for each dataset/model/feature combination from the updated PIPE runs. The total posterior is $\ln \mathcal{L} = \ln \mathcal{L}_{\text{KDE}} + \ln \pi_r$; the Taylor penalty is zero for all listed best fits.

Dataset	Model	A_s	r	n_s	α_s	β_s
ACT+P	Powerlaw	2.1367×10^{-9}	0.0291	0.9779	-4.09×10^{-4}	-8.81×10^{-6}
	Powerlaw+Gaussian-Bump	2.1109×10^{-9}	0.0125	0.9680	-4.15×10^{-4}	-6.46×10^{-6}
	Powerlaw+Gaussian-Dip	2.1110×10^{-9}	0.0125	0.9680	-4.12×10^{-4}	-6.39×10^{-6}
	Axion-Monodromy	2.1235×10^{-9}	0.0125	0.9713	$+3.70 \times 10^{-3}$	-5.13×10^{-4}
ACT+P+SPT	Powerlaw	2.1092×10^{-9}	0.0227	0.9787	-3.94×10^{-4}	-8.27×10^{-6}
	Powerlaw+Gaussian-Bump	2.1209×10^{-9}	0.0130	0.9681	$+2.94 \times 10^{-3}$	-2.92×10^{-4}
	Powerlaw+Gaussian-Dip	2.1209×10^{-9}	0.0130	0.9681	$+2.96 \times 10^{-3}$	-2.96×10^{-4}
	Axion-Monodromy	2.1209×10^{-9}	0.0125	0.9681	$+2.96 \times 10^{-3}$	-2.95×10^{-4}
ACT+P+SPT+eBOSS	Powerlaw	2.1547×10^{-9}	0.1210	0.9665	-6.16×10^{-4}	-1.65×10^{-5}
	Powerlaw+Gaussian-Bump	2.1293×10^{-9}	0.0125	0.9693	-8.66×10^{-3}	-2.56×10^{-3}
	Powerlaw+Gaussian-Dip	2.1293×10^{-9}	0.0125	0.9693	-8.66×10^{-3}	-2.56×10^{-3}
	Axion-Monodromy	2.1293×10^{-9}	0.0125	0.9693	-8.66×10^{-3}	-2.56×10^{-3}

TABLE II. Verified spectral parameters from the best-fit potentials. All quantities are evaluated at the pivot scale $k_* = 0.05 \text{ Mpc}^{-1}$.

servables, or even trigger phases of ultra-slow roll leading to primordial black hole formation [32]. We model such effects by modulating the baseline potential with

$$V = V_\alpha \left[1 \pm A \exp \left(-\frac{(\phi - \phi_0)^2}{2\sigma^2} \right) \right], \quad (2)$$

where the + sign produces a bump and the - a dip. The parameters A , ϕ_0 , and σ set the amplitude, position, and width, controlling the induced running and feature scale.

Axion monodromy. Inspired by axion-like inflation in string theory [33, 34], monodromy potentials also include periodic modulations on a monomial background:

$$V = V_0 \left[\left| \frac{\phi}{M_p} \right|^\alpha + A \cos \left(\gamma + \frac{M_p}{f} \left| \frac{\phi}{M_p} \right|^{1+p_f} \right) \right], \quad (3)$$

with amplitude A , phase γ , axion decay constant f , and index p_f . These oscillations naturally generate small-scale running and resonant signatures in the PPS.

Inflation Observables. For each benchmark model and parameter set, we computed the PPS amplitude A_s , spectral index n_s , tensor-to-scalar ratio r , and scale dependence parameters α_s and β_s by integrating the background equations numerically. The slow-roll parameters were evaluated analytically from the potential and its derivatives at horizon exit, to leading order in the slow-roll expansion [35]. The PPS was then reconstructed on all relevant scales using the slow-roll approximation.

Parameter choices for which the Taylor expansion of Eq. (1)—employed in the previous section to infer posteriors for $\{A_s, n_s, \alpha_s, \beta_s\}$ —failed to reproduce the spectrum up to the eBOSS scales were discarded (see Supplemental Material for details).

Dataset	Model	$\Delta \chi^2$	ΔAIC
ACT+P	Powerlaw+Bump	-7.27	-1.27
	Powerlaw+Dip	-7.27	-1.27
	Axion-Monodromy	-7.27	0.73
+SPT	Powerlaw+Bump	-5.52	0.48
	Powerlaw+Dip	-5.52	0.48
	Axion-Monodromy	-5.57	2.43
+eBOSS	Powerlaw+Bump	-107.09	-101.09
	Powerlaw+Dip	-107.09	-101.09
	Axion-Monodromy	-107.09	-99.09

TABLE III. Statistical deviation of the best-fit feature and axion-monodromy models relative to the baseline power-law potential for each dataset combination. Negative ΔAIC values indicate statistical preference over the baseline model. The likelihood difference is defined as $\Delta \chi^2 = -2(\ln \mathcal{L}_{\text{model}} - \ln \mathcal{L}_{\text{powerlaw}})$.

Likelihood. To compare model predictions with CMB and LSS data, we build a custom likelihood over the effective PPS parameters $\{A_s, n_s, \alpha_s, \beta_s\}$. Posterior samples from the MCMC chains are processed with `GetDist` [36] and approximated by a multidimensional Gaussian ker-

nel density estimator (KDE), defining a smooth empirical likelihood $\ln \mathcal{L}_{\text{KDE}}(A_s, n_s, \alpha_s, \beta_s)$. These procedures are implemented in our public code **PIPE** (Potential Inflation Posterior Emulator), which provides a fast surrogate for the full CMB and eBOSS likelihoods (see Supplemental Material).

Although the analysis focuses on the scalar spectrum, **PIPE** also enforces consistency with current bounds on the tensor-to-scalar ratio by adding a BK18-based prior $\ln \pi_r$ [37] to the log-likelihood.

Best-Fit Search. For each dataset, we maximized the **PIPE** log-posterior $\ln \mathcal{P} \equiv \ln \mathcal{L}_{\text{KDE}} + \ln \pi_r$ under broad, uninformative priors on the model parameters. The optimisation combined a Genetic Algorithm (**evortran** [38]) with a final Nelder–Mead refinement. For every dataset–model–feature combination we repeated the GA with different random seeds and retained the best posterior value. This procedure yields robust potential constraints and enables consistency checks across the P–ACT, P–ACT+SPT, and P–ACT+SPT+eBOSS combinations.

Results. The best-fit potentials and spectral parameters are listed in Tables I–II. Because multiple parameter combinations yield nearly identical effective spectra ($A_s, n_s, \alpha_s, \beta_s$), the KDE posterior exhibits flat regions with equivalent maxima; we therefore quote a representative best-fit per model and dataset. Likelihood–ratio tests relative to the baseline power law give the $\Delta\chi^2$ and ΔAIC values in Table III. For CMB data alone (ACT+P and ACT+P+SPT), the extensions provide only mild improvements, with $|\Delta\chi^2| \simeq 5\text{--}7$ and small $|\Delta\text{AIC}| \lesssim 2$. When eBOSS data are included, the power-law potential becomes strongly disfavoured, while all featureful and axion–monodromy models achieve comparable maximum posteriors around $\ln \mathcal{L} \simeq 40.9$. The identical likelihoods of these feature models reflect the Taylor-expansion consistency condition, which constrains them to the same smooth slow-roll branch of the potential.

Summary and Discussion. — We investigated whether the latest combination of Planck, ACT, SPT-3G, and eBOSS Ly- α data supports departures from a power-law primordial spectrum and which inflationary potentials can reproduce the observed scale dependence. Using a two-step procedure—(i) deriving posteriors for $\{A_s, n_s, \alpha_s, \beta_s\}$ and (ii) constructing a fast surrogate likelihood implemented in the public code **PIPE**⁴—we scanned four representative single-field potentials (power-law, dip, bump, and axion-monodromy) and identified their best-fit configurations for different dataset combinations.

For CMB data alone, a simple power-law spectrum remains fully adequate: the inferred runnings are consistent with zero, and high- ℓ measurements show no evidence for strong scale dependence. Feature and

axion–monodromy extensions yield only mild improvements, with $|\Delta\chi^2| \simeq 5\text{--}7$ (where $\Delta\chi^2 = -2\Delta \ln \mathcal{L}$) and $|\Delta\text{AIC}| \lesssim 2$, confirming that the CMB data are well described by a nearly scale-invariant spectrum.

When eBOSS Ly- α data are included, the situation changes strikingly. The power-law model becomes strongly disfavoured ($\ln \mathcal{L} = -12.6$), while all featureful and monodromy potentials achieve comparable posteriors around $\ln \mathcal{L} \simeq 40.9$, with $\Delta\chi^2 \simeq -107$ and $\Delta\text{AIC} \simeq -100$ relative to the baseline. These models fit the observed small-scale suppression through negative running and non-zero running of the running, as summarised in Table II. Their identical likelihoods arise from the Taylor-expansion condition, which confines them to the same smooth slow-roll branch of the potential.

These results highlight a persistent tension between high- ℓ CMB data—consistent with near-scale invariance—and Ly- α measurements, which require a suppression of small-scale power. Localised features in the inflaton potential, whether represented phenomenologically as Gaussian bumps/dips or as axion–monodromy modulations, provide an equally good description of the combined data. We stress that, although we restricted ourselves to power-law baseline potentials, none of the standard slow-roll models, including α -attractors, produce such large higher-order runnings, implying that the improvement originates from localised structures in the potential.

While alternative late-time explanations (e.g. a small warm-DM fraction [7]) can mimic a smooth cutoff in the matter power spectrum [39–44], our analysis demonstrates that the existing eBOSS–CMB tension can also be ameliorated by physics at the inflationary scale, even when the potentials considered are restricted to those which can be captured by a Taylor expansion around the pivot scale. It would be interesting to see in the future whether more general potentials could alleviate the discrepancy further. If confirmed by next-generation LSS and small-scale CMB surveys, these results may constitute indirect evidence of high-energy structures in the inflaton potential.

ACKNOWLEDGEMENTS

The authors would like to thank Hengameh Bagherian, Jo Dunkley, and Mudit Jain for helpful discussions throughout this project, as well as Doddy Marsh and Keir Rogers for valuable comments on our manuscript. They are also grateful to Thomas Biekötter for his assistance with the **evortran** code. This work was supported by the STFC under UKRI grant ST/X000753/1. LH also thanks the Institute for Particle Physics Phenomenology at Durham University for access to its high-performance computing facilities.

⁴ gitlab.com/cosmoPipe/pipe-inflation

[1] A. R. Liddle and D. H. Lyth, *Phys. Rept.* **231**, 1 (1993), [arXiv:astro-ph/9303019](https://arxiv.org/abs/astro-ph/9303019).

[2] D. Baumann, *Cosmology* (Cambridge University Press, 2022).

[3] A. H. Guth, *Phys. Rev. D* **23**, 347 (1981).

[4] E. Komatsu *et al.* (WMAP), *Astrophys. J. Suppl.* **192**, 18 (2011), [arXiv:1001.4538 \[astro-ph.CO\]](https://arxiv.org/abs/1001.4538).

[5] N. Aghanim *et al.* (Planck), *Astron. Astrophys.* **641**, A6 (2020), [Erratum: *Astron. Astrophys.* 652, C4 (2021)], [arXiv:1807.06209 \[astro-ph.CO\]](https://arxiv.org/abs/1807.06209).

[6] S. Chabanier *et al.* (eBOSS), *JCAP* **07**, 017 (2019), [arXiv:1812.03554 \[astro-ph.CO\]](https://arxiv.org/abs/1812.03554).

[7] K. K. Rogers and V. Poulin, *Phys. Rev. Res.* **7**, L012018 (2025), [arXiv:2311.16377 \[astro-ph.CO\]](https://arxiv.org/abs/2311.16377).

[8] T. Louis *et al.* (ACT), (2025), [arXiv:2503.14452 \[astro-ph.CO\]](https://arxiv.org/abs/2503.14452).

[9] E. Calabrese *et al.* (ACT), (2025), [arXiv:2503.14454 \[astro-ph.CO\]](https://arxiv.org/abs/2503.14454).

[10] S. Hannestad, S. H. Hansen, F. L. Villante, and A. J. S. Hamilton, *Astropart. Phys.* **17**, 375 (2002), [arXiv:astro-ph/0103047](https://arxiv.org/abs/astro-ph/0103047).

[11] E. Camphuis *et al.* (SPT-3G), (2025), [arXiv:2506.20707 \[astro-ph.CO\]](https://arxiv.org/abs/2506.20707).

[12] N. Aghanim *et al.* (Planck), *Astron. Astrophys.* **641**, A5 (2020), [arXiv:1907.12875 \[astro-ph.CO\]](https://arxiv.org/abs/1907.12875).

[13] L. Pagano, J. M. Delouis, S. Mottet, J. L. Puget, and L. Vibert, *Astron. Astrophys.* **635**, A99 (2020), [arXiv:1908.09856 \[astro-ph.CO\]](https://arxiv.org/abs/1908.09856).

[14] S. Goldstein, J. C. Hill, V. Iršič, and B. D. Sherwin, *Phys. Rev. Lett.* **131**, 201001 (2023), [arXiv:2303.00746 \[astro-ph.CO\]](https://arxiv.org/abs/2303.00746).

[15] J. Torrado and A. Lewis, *JCAP* **05**, 057 (2021), [arXiv:2005.05290 \[astro-ph.IM\]](https://arxiv.org/abs/2005.05290).

[16] A. Lewis, A. Challinor, and A. Lasenby, *Astrophys. J.* **538**, 473 (2000), [arXiv:astro-ph/9911177](https://arxiv.org/abs/astro-ph/9911177).

[17] M. Raveri and C. Doux, *Phys. Rev. D* **104**, 043504 (2021), [arXiv:2105.03324 \[astro-ph.CO\]](https://arxiv.org/abs/2105.03324).

[18] R. Kallosh, A. Linde, and D. Roest, *JHEP* **11**, 198 (2013), [arXiv:1311.0472 \[hep-th\]](https://arxiv.org/abs/1311.0472).

[19] R. Kallosh, A. Linde, and D. Roest, *JHEP* **08**, 052 (2014), [arXiv:1405.3646 \[hep-th\]](https://arxiv.org/abs/1405.3646).

[20] R. Kallosh and A. Linde, *JCAP* **10**, 033 (2013), [arXiv:1307.7938 \[hep-th\]](https://arxiv.org/abs/1307.7938).

[21] A. A. Starobinsky, *Phys. Lett. B* **91**, 99 (1980).

[22] F. L. Bezrukov and M. Shaposhnikov, *Phys. Lett. B* **659**, 703 (2008), [arXiv:0710.3755 \[hep-th\]](https://arxiv.org/abs/0710.3755).

[23] E. G. M. Ferreira, E. McDonough, L. Balkenhol, R. Kallosh, L. Knox, and A. Linde, (2025), [arXiv:2507.12459 \[astro-ph.CO\]](https://arxiv.org/abs/2507.12459).

[24] M. Drees and Y. Xu, *Phys. Lett. B* **867**, 139612 (2025), [arXiv:2504.20757 \[astro-ph.CO\]](https://arxiv.org/abs/2504.20757).

[25] M. R. Haque, S. Pal, and D. Paul, (2025), [arXiv:2505.04615 \[astro-ph.CO\]](https://arxiv.org/abs/2505.04615).

[26] D. S. Zharov, O. O. Sobol, and S. I. Vilchinskii, *Phys. Rev. D* **112**, 023544 (2025).

[27] Y.-Y. Ye and B.-M. Gu, (2025), [arXiv:2507.20307 \[gr-qc\]](https://arxiv.org/abs/2507.20307).

[28] N. Barnaby and Z. Huang, *Phys. Rev. D* **80**, 126018 (2009), [arXiv:0909.0751 \[astro-ph.CO\]](https://arxiv.org/abs/0909.0751).

[29] N. Barnaby, *Phys. Rev. D* **82**, 106009 (2010).

[30] D. J. H. Chung, E. W. Kolb, A. Riotto, and I. I. Tkachev, *Phys. Rev. D* **62**, 043508 (2000), [arXiv:hep-ph/9910437](https://arxiv.org/abs/hep-ph/9910437).

[31] J. Fumagalli, S. Renaux-Petel, and L. T. Witkowski, *JCAP* **08**, 030 (2021), [arXiv:2012.02761 \[astro-ph.CO\]](https://arxiv.org/abs/2012.02761).

[32] S. S. Mishra and V. Sahni, *JCAP* **04**, 007 (2020), [arXiv:1911.00057 \[gr-qc\]](https://arxiv.org/abs/1911.00057).

[33] R. Flauger, L. McAllister, E. Pajer, A. Westphal, and G. Xu, *JCAP* **06**, 009 (2010), [arXiv:0907.2916 \[hep-th\]](https://arxiv.org/abs/0907.2916).

[34] R. Flauger, L. McAllister, E. Silverstein, and A. Westphal, *JCAP* **10**, 055 (2017), [arXiv:1412.1814 \[hep-th\]](https://arxiv.org/abs/1412.1814).

[35] P. Auclair and C. Ringeval, *Phys. Rev. D* **106**, 063512 (2022), [arXiv:2205.12608 \[astro-ph.CO\]](https://arxiv.org/abs/2205.12608).

[36] A. Lewis, (2019), [arXiv:1910.13970 \[astro-ph.IM\]](https://arxiv.org/abs/1910.13970).

[37] M. Tristram *et al.*, *Phys. Rev. D* **105**, 083524 (2022), [arXiv:2112.07961 \[astro-ph.CO\]](https://arxiv.org/abs/2112.07961).

[38] T. Biekötter, (2025), [arXiv:2507.06082 \[hep-ph\]](https://arxiv.org/abs/2507.06082).

[39] M. Archidiacono, D. C. Hooper, R. Murgia, S. Bohr, J. Lesgourgues, and M. Viel, *JCAP* **10**, 055 (2019), [arXiv:1907.01496 \[astro-ph.CO\]](https://arxiv.org/abs/1907.01496).

[40] H. Bagherian, M. Joseph, M. Schmaltz, and E. N. Sivarajan, *Phys. Rev. D* **111**, 043513 (2025), [arXiv:2405.17554 \[astro-ph.CO\]](https://arxiv.org/abs/2405.17554).

[41] M.-Y. Wang, R. A. C. Croft, A. H. G. Peter, A. R. Zentner, and C. W. Purcell, *Phys. Rev. D* **88**, 123515 (2013).

[42] D. C. Hooper, N. Schöneberg, R. Murgia, M. Archidiacono, J. Lesgourgues, and M. Viel, *JCAP* **10**, 032 (2022), [arXiv:2206.08188 \[astro-ph.CO\]](https://arxiv.org/abs/2206.08188).

[43] N. Palanque-Delabrouille *et al.*, *JCAP* **11**, 011 (2015), [arXiv:1506.05976 \[astro-ph.CO\]](https://arxiv.org/abs/1506.05976).

[44] A. He, M. M. Ivanov, S. Bird, R. An, and V. Gluscevic, *Phys. Rev. D* **112**, 063540 (2025).

[45] S. Chabanier, M. Millea, and N. Palanque-Delabrouille, *Mon. Not. Roy. Astron. Soc.* **489**, 2247 (2019), [arXiv:1905.08103 \[astro-ph.CO\]](https://arxiv.org/abs/1905.08103).

[46] A. H. Wright *et al.*, (2025), 10.1051/0004-6361/202554908, [arXiv:2503.19441 \[astro-ph.CO\]](https://arxiv.org/abs/2503.19441).

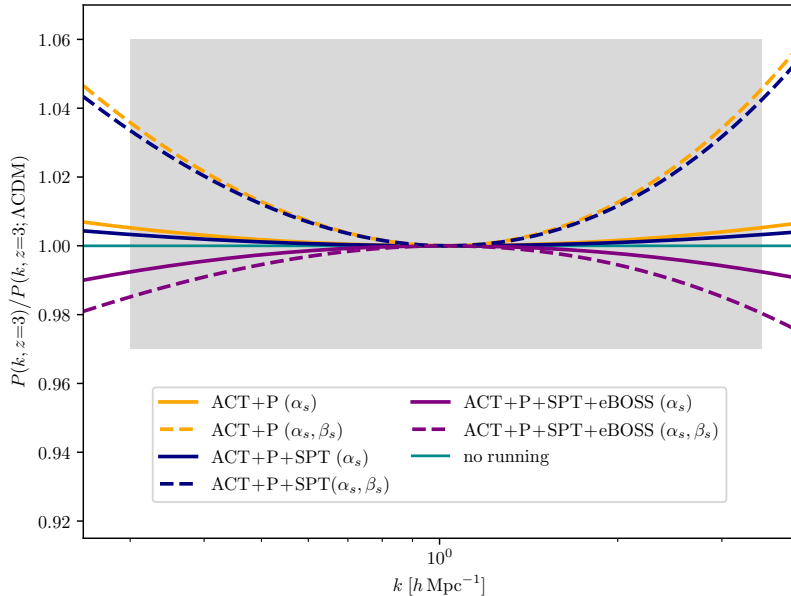


FIG. S1. Linear matter power spectrum, rescaled both in amplitude and scale compared to the ΛCDM best fit from *Planck* [5] at the eBOSS scale, and compared to the eBOSS range of frequencies and credible region (grey-shaded area) as defined in Ref. [45].

Supplemental Material

S1. VALIDITY OF THE EBOSS LIKELIHOOD

To assess the validity of the compressed eBOSS likelihood we used in the analysis, we checked that the linear matter power spectrum obtained remains sufficiently close to a power-law, within the 1σ validity band of the eBOSS measurement. To do so, we used a similar approach as in Ref. [7], by taking the best-fit linear matter power spectra for each dataset combination, and rescaling them such that they have the same values of Δ_{lin}^2 , n_{lin} as the best-fit ΛCDM model from *Planck* [5] at the eBOSS scale. Results are depicted in FIG. S1, where one can see that each best fit point leads to a linear matter power spectrum that is contained within the eBOSS range of frequencies and credible region, as calculated in Ref. [45] (grey-shaded area), meaning that the linear matter power spectrum obtained is sufficiently power-law-like for the eBOSS compression to remain valid over the appropriate range of scales.

S2. TAYLOR EXPANSION

When confronting power spectra obtained from slow-roll inflation potentials, we used the Taylor expansion of Eq. (1) at the pivot scale, and assumed that this expansion is valid up to the eBOSS scale $k \simeq 1 \text{ hMpc}^{-1}$, so we can use the constraints on $\{A_s, n_s, \alpha_s, \beta_s\}$ obtained from CMB and Ly- α likelihoods to constrain potential parameters. To assess the validity of this assumption, we calculated the PPS using the slow-roll approximation numerically and compared its value at the eBOSS scale. We imposed the relative difference to be within $\delta \equiv |\Delta_{\mathcal{R}, \text{Taylor}}^2 - \Delta_{\mathcal{R}}^2|/\Delta_{\mathcal{R}}^2 < \delta_{\text{thresh}}$, where we chose $\delta_{\text{thresh}} = 1\%$ so that the corresponding error made on the linear matter power spectrum at the eBOSS scale lies within the 1σ sensitivity bound of the eBOSS measurement that is of order $\mathcal{O}(10)\%$ [45]. To enforce this condition while guiding the genetic algorithm to the right region of the parameter space, we added to the likelihood an extra contribution

$$\Delta \mathcal{L}_{\text{Taylor}} = \begin{cases} \left(\frac{\delta - \delta_{\text{thresh}}}{\delta_{\text{thresh}}} \right)^p & \text{if } \delta > \delta_{\text{thresh}} \\ 0 & \text{if } \delta < \delta_{\text{thresh}} \end{cases}, \quad (\text{S1})$$

Furthermore, because the eBOSS data spans a larger range of frequencies, we also demanded that this error does not exceed 3% at $k_{\text{eBOSS, max}} \approx 3.5 \text{ hMpc}^{-1}$. We checked that every best fit found by the algorithm lies within the region

where $\Delta\mathcal{L}_{\text{Taylor}} = 0$, so that this guiding penalty does not contribute to the value of the likelihood. In our analysis, we used $p = 2$, although our code allows for choosing arbitrary values of p , δ_{thresh} , and the possibility to adding an additional pre-factor to the penalty.

S3. PIPE: POTENTIAL INFLATION POSTERIOR EMULATOR

To streamline the comparison between theoretical predictions and observational constraints, we developed a public Python package called PIPE (Potential Inflation Posterior Emulator), which can be found in

gitlab.com/cosmoPipe/pipe-inflation. (S2)

PIPE provides a fast, data-driven likelihood for inflationary models by emulating the joint posterior of effective spectral parameters $(A_s, n_s, \alpha_s, \beta_s)$ from the P-ACT, P-ACT+SPT, and P-ACT+SPT+eBOSS datasets. The code reads in `GetDist` MCMC chains of effective parameters and constructs a smoothed empirical likelihood via a Gaussian kernel density estimator (KDE) with a bandwidth tuned for each dataset according to Scott's rule. It then allows the user to specify either built-in or fully custom inflationary potentials; for each parameter point θ , PIPE evolves the background equations and returns the predicted spectral parameters $[A_s, r, n_s, \alpha_s, \beta_s]$ at leading order in slow roll, following Ref. [35]. These predictions are directly evaluated against the KDE likelihood to obtain $\ln\mathcal{L}_{\text{KDE}}$, optionally combined with an r -prior $\ln\pi_r$ from BK18 via `LogL_r.py`, yielding the total log-posterior $\ln\mathcal{L}_{\text{KDE}} + \ln\pi_r$. A Taylor-expansion penalty is also implemented (as described in S2).

Internally, PIPE consists of:

- `pipe/Inflation_evo.py`, which computes $[A_s, r, n_s, \alpha_s, \beta_s]$ for supported and user-provided potentials.
- `pipe/LogL_KDE.py`, which constructs the KDE likelihood directly from `GetDist` chains.
- `pipe/LogL_r.py`, which configures the BK18 r -prior [37].
- `example/example.py`, an end-to-end demonstration showing how to use the built-in `Powerlaw` model with the same custom potential, and compute $\ln\mathcal{L}_{\text{KDE}}$ all the contributions to the likelihood.

Built-in templates include `Powerlaw` (with optional Gaussian-dip or bump features) and `Monodromy`; new models can be added by providing the potential and its first four derivatives.

Fig. S2 shows, for the P-ACT+EPT+eBOSS dataset, a direct comparison between the raw `GetDist` chains (black outlines) and their KDE approximation (purple fill) produced with PIPE, illustrating how the KDE accurately reproduces the full MCMC posterior used in our analysis.

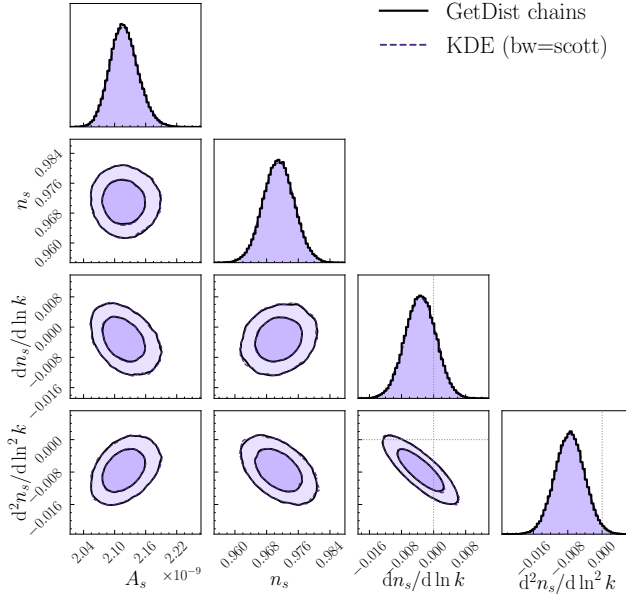


FIG. S2. Comparison for the P-ACT+SPT+eBOSS dataset of the 1D and 2D posterior distributions for the effective inflationary parameters $\{A_s, n_s, \alpha_s, \beta_s\}$ obtained directly from the `GetDist` chains (black outlines) and from a Gaussian KDE resampling (purple fill) using our public `PIPE` code. The band width has been set according to the Scott's rule.

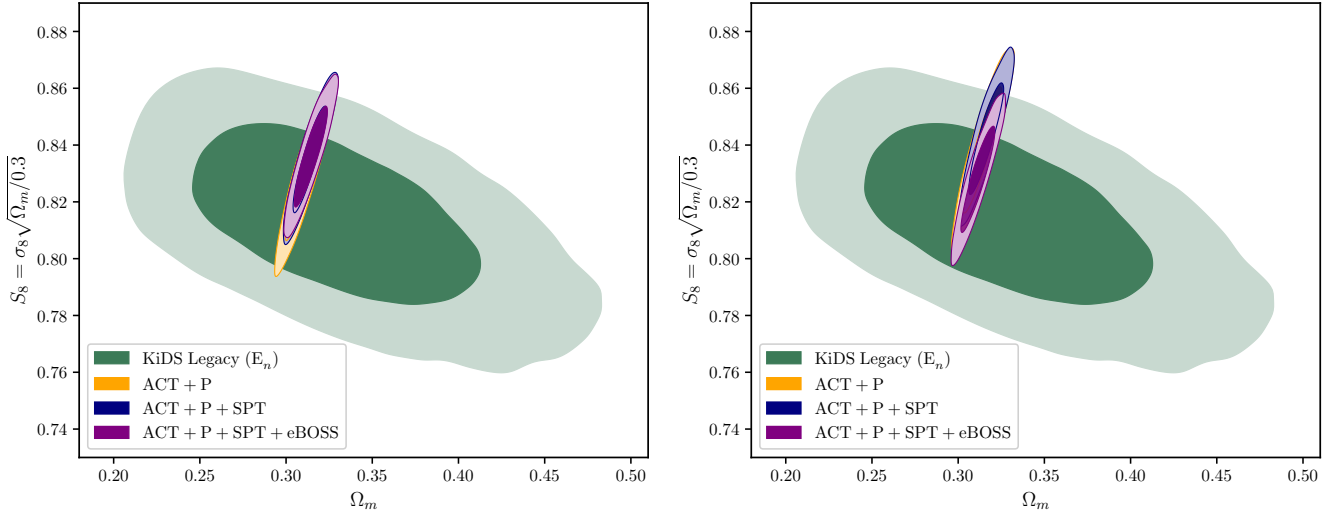


FIG. S3. Posteriors for Ω_m, S_8 when includin the running (left panel) and running-of-the-running (right panel) of the spectral index. For comparison, green contours depict the credible region, as preferred by KiDS Legacy [46].

S4. EFFECT ON σ_8

We survey here to which extent the running of the PPS's spectral index favoured by the CMB datasets considered affect the value of σ_8 and compare it to the existing constraints from KiDS Legacy [46]. As one can see from FIG. S3, inclusion of the running and running of the running affect very mildly the σ_8 and remains consistent with current data, with SPT asking for a slightly larger σ_8 than ACT. The discrepancy remains between the CMB values and the other weak lensing surveys, but the tension is not significantly altered when we include the running considered in this work.

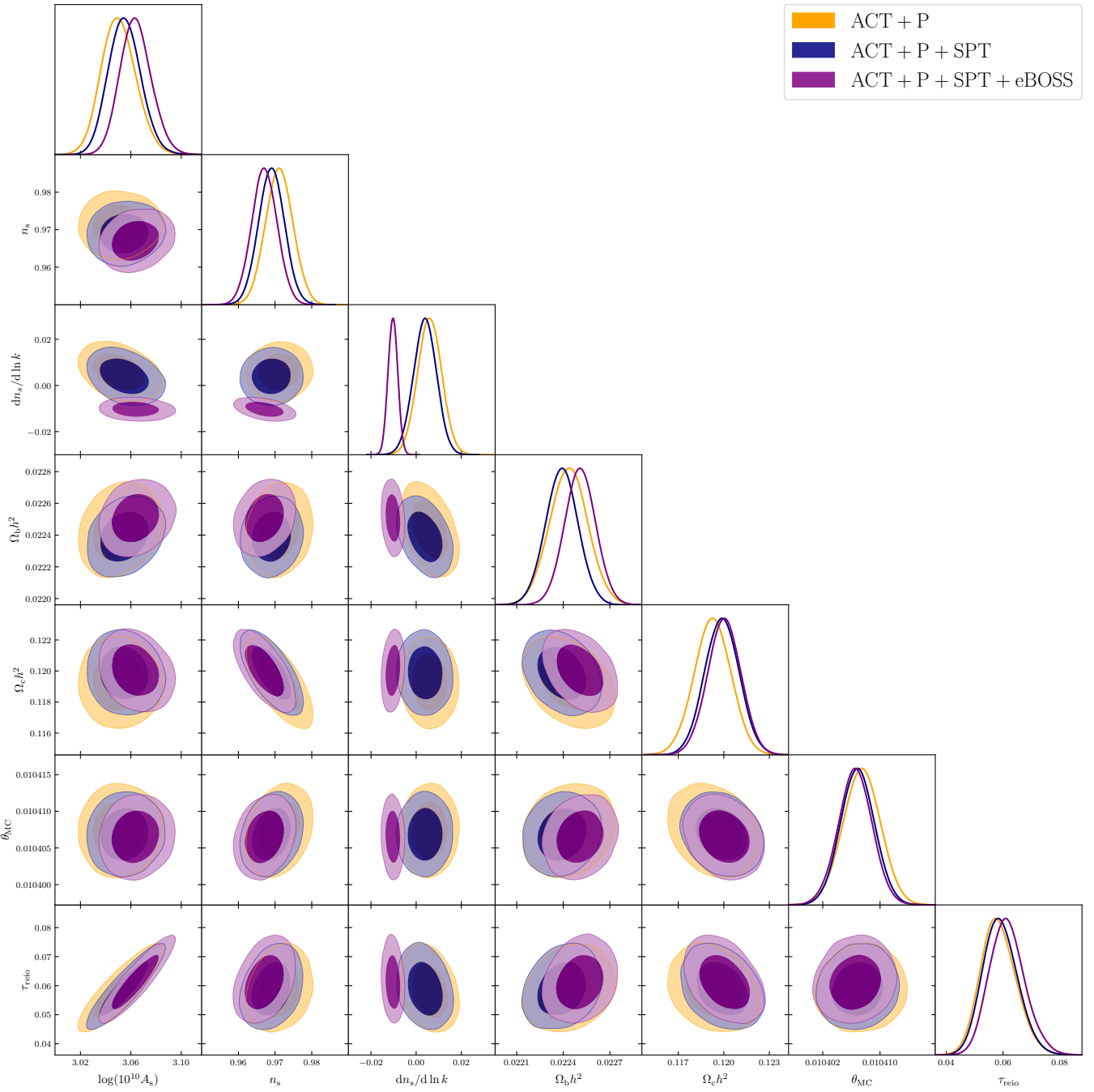


FIG. S4. Full cosmological 1D and 2D posteriors obtained when including the running of the spectral index α_s .

S5. FULL COSMOLOGICAL RESULTS

We report in FIG. S4 and S5 the full 1D and 2D cosmological posteriors obtained when including either α_s or α and β_s in our analysis.

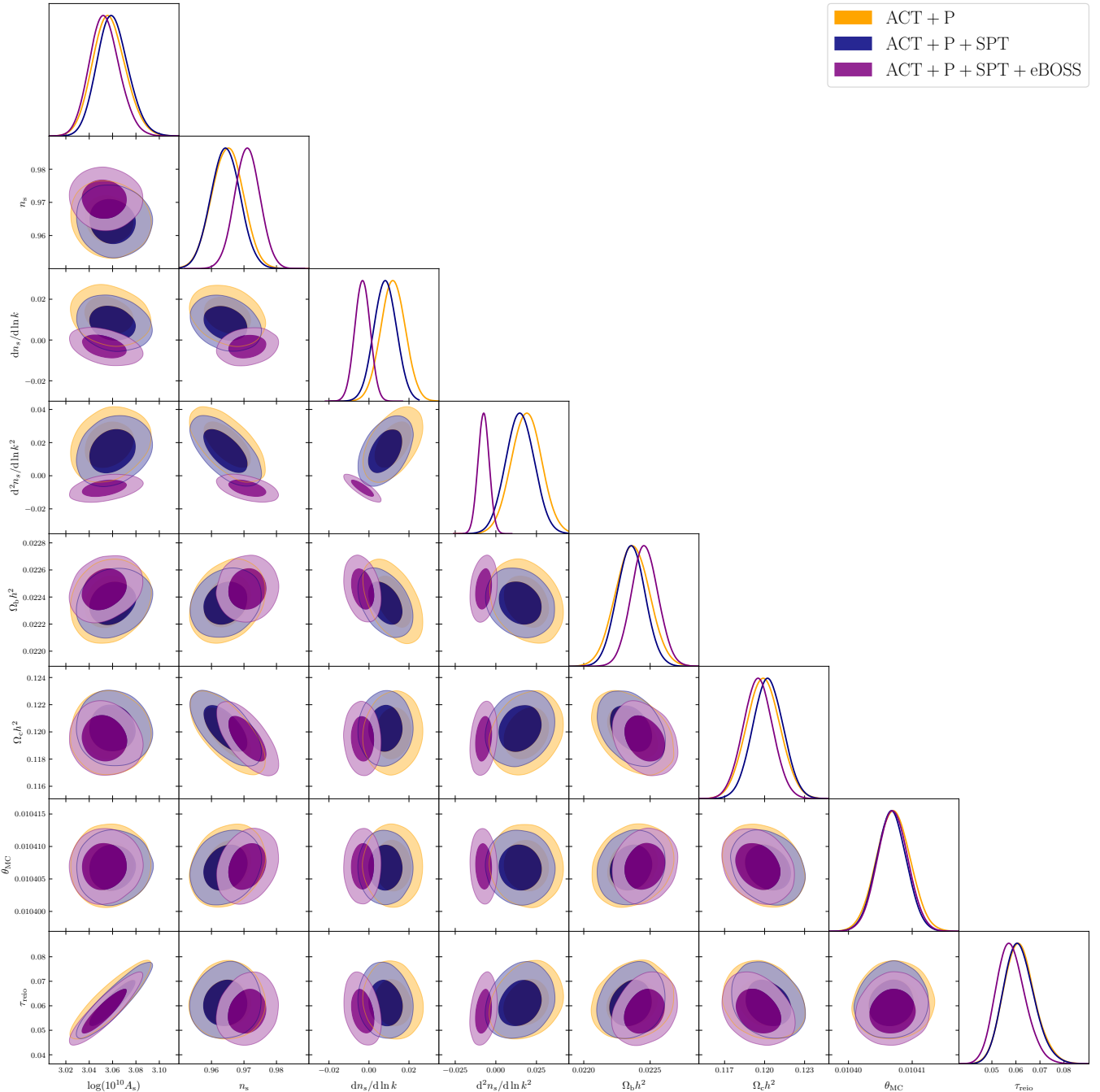


FIG. S5. Full cosmological 1D and 2D posteriors obtained when including the running of the spectral index α_s , and the running-of-the-running β_s .

Dataset	n_s	α_s	β_s
ACT+P	$0.96501^{+0.00490}_{-0.00493}$	$0.01195^{+0.00623}_{-0.00628}$	$0.01869^{+0.00954}_{-0.00967}$
+ SPT	$0.96437^{+0.00453}_{-0.00449}$	$0.00804^{+0.00567}_{-0.00571}$	$0.01477^{+0.00884}_{-0.00876}$
+ eBOSS	$0.97101^{+0.00391}_{-0.00388}$	$-0.00323^{+0.00390}_{-0.00388}$	$-0.00755^{+0.00346}_{-0.00347}$

TABLE IV. Median values and 68% credible intervals (16th and 84th percentiles) for n_s , α_s , and β_s in three data combinations: ACT+Planck (ACT+P), with added SPT data (+SPT), and with both SPT and eBOSS data (+eBOSS).

S6. PIMORDIAL POWER SPECTRUM MEDIAN VALUES AND STATISTICAL TENSIONS WITH Λ CDM

The median values and 68% credible intervals (16th and 84th percentiles) for n_s , α_s , and β_s obtained from different dataset combinations are listed in TABLE IV. For the case of Λ CDM, and when including either the running alone (α_s) or both the running and running-of-the-running (β_s) of the spectral index, we used the package `tensiometer` [17] to estimate the statistical tension between CMB observatories and eBOSS measurements. This package allows to calculate the statistical tension between distributions that are not necessarily gaussian, which is exactly what is needed in our case. In each case, we tested that the result obtained is stable when varying internal settings used by `tensiometer`, such as the smoothing scale used in the estimate of the KDE shift—integrated square error (MISE), adaptive bandwidth (BALL), asymptotic MISE estimator (AMISE), or maximum bandwidth (MAX)—or the *boost* sampling parameter, which we varied to larger and larger values until obtaining a stable result. Our results are presented in TABLE V. Note that, in the case of Λ CDM, `tensiometer` failed at returning either a stable or finite result, due to the too small overlap between the CMB and eBOSS distributions. Some finite results returned were above 5.7σ , which allowed us to safely claim a tension larger than 5σ both for ACT+P and ACT+P+SPT.

Dataset	Λ CDM	$+ \alpha_s$	$+ (\alpha_s, \beta_s)$
P-ACT	$\gg 5\sigma$	$3.375^{+0.002}_{-0.002}\sigma$	$3.074^{+0.001}_{-0.001}\sigma$
+SPT	$\gg 5\sigma$	$3.038^{+0.001}_{-0.001}\sigma$	$2.813^{+0.001}_{-0.001}\sigma$

TABLE V. Statistical tension between different CMB dataset combinations: Planck+ACT (P-ACT), with added SPT data (+SPT), and eBOSS data (+eBOSS).